HYDROMAGNETIC TURBULENT FLOW IN POROUS MEDIA OVER A STRETCHING SURFACE IN A ROTATING SYSTEM WITH HEAT

Abstract

This study investigates the combined effects of magnetic fields, buoyancy forces, porosity, rotation, and Joule's heating on fluid flow and heat transfer dynamics. The analysis is performed using a numerical approach, with the system oriented along three axes: the z-axis aligned with the plate, the y-axis perpendicular to the plate, and the x-axis orthogonal to the y-z plane. An infinite plate extends along the x and z axes, with a uniform transverse magnetic field applied parallel to the y-axis. By employing the finite difference method in MATLAB, we explore how various dimensionless parameters influence temperature and velocity profiles.

Our findings reveal that an increase in the local temperature Grashof number enhances primary velocity while reducing secondary velocity near the fixed end. Temperature profiles show a decrease near the plate, increasing further away. The study also highlights that a higher Joule heating parameter leads to elevated primary velocity and temperature profiles but diminishes secondary velocity. Additionally, increasing rotational parameters is observed to decrease both primary and secondary velocities while augmenting temperature profiles near the plate.

These results underscore the significant role that magnetic fields, rotational effects, and Joule heating play in modulating fluid flow and thermal behavior. The insights gained from this study can inform the design and optimization of engineering systems where control of velocity and temperature profiles is critical.

Key words: Magnetic field, buoyancy force, porosity, Joule's heating, rotational parameter, primary and secondary velocities.

Introduction

The production of sheeting materials, including both metal and polymer sheets, is integral to various industrial manufacturing processes. The fluid dynamics associated with a stretching surface have significant applications in numerous engineering processes. For instance, many technical processes involving polymers require the cooling of continuous strips extruded from a die by drawing them through a stagnant fluid with a controlled cooling system. As these strips are drawn, their surfaces may be stretched, and the quality of the final product depends on the rate of heat transfer on the stretching surface (Mahapatra & Gupta , 2004). Therefore, controlling the cooling rate is essential to achieving the desired quality of the final product.

Stretching surfaces have numerous real-life applications across various fields. In polymer processing industries, stretching surfaces are encountered in extrusion, injection molding, and blow molding processes, where the stretching of polymer materials affects their mechanical properties and final product characteristics. In biomedical engineering, stretching surfaces are crucial in tissue engineering and regenerative medicine, where tissue scaffolds provide controlled stretching to promote cell growth and tissue regeneration. In the papermaking industry, pulp fibers undergo stretching and deformation on moving surfaces during the drying and pressing stages, significantly influencing the final paper product's strength, smoothness, and other properties. Textile production involves stretching surfaces in processes like weaving, knitting, and dyeing, affecting fabrics' tensile strength, elasticity, and overall quality.

Porosity, the measure of void spaces in a material, has diverse applications across different fields. In construction, porous materials such as concrete and bricks allow water to seep through, reducing runoff and facilitating groundwater recharge, while bricks with controlled porosity offer better thermal insulation and moisture control. Porous materials like aerogels, foams, and fiberglass are used for thermal insulation in buildings, refrigeration systems, and aerospace applications, where the trapped air within the porous structure reduces heat transfer, enhancing energy efficiency. In oil and gas recovery, porous reservoir rocks such as sandstone and limestone are essential for extracting hydrocarbons, as the interconnected pore network allows for the storage and flow of these resources. Porous acoustic materials like acoustic foams and panels are used for noise control in architectural, automotive, and industrial applications, where the porous structure dissipates sound energy through absorption and damping.

In the agricultural sector, porous soil aggregates promote water infiltration, root growth, and nutrient uptake, influencing soil fertility, drainage, aeration, and overall crop production rate and ecosystem health. For energy storage, porous electrodes are used in batteries, fuel cells, and supercapacitors, where the high surface area and interconnected pore network enhance ion transport and electrochemical reactions, improving device performance. Recent advancements in understanding porous media flows have also been leveraged in the design and production of industrial equipment and computer disk drives (Singh & Jha, 2013).

Considerable interest has been given to the theory of rotating fluids due to its applications in cosmic and geophysical sciences. Numerous studies have been conducted on boundary layer flows of viscous fluids due to uniformly stretching sheets. For instance (Giterere, 2013) investigated the behavior of boundary layer flows over a stretching sheet, focusing on the effects of viscosity and thermal conductivity. The study found that these properties significantly influence the rate of heat transfer and the stability of the boundary layer. Similarly, Srihari (2021) extended this analysis by considering the impact of magnetic fields on the flow, concluding that magnetic fields can be used to control the rate of heat transfer, providing a potential method for optimizing cooling processes in industrial applications.

Further research has explored the interaction between stretching surfaces and rotating fluids. For example, Kumari & Gorla (2015) discovered that rotation introduces additional complexity to flow patterns and heat transfer rates, which must be carefully managed to ensure product quality in manufacturing processes.

Ngari (2017) also studied the effects of suction and injection on the boundary layer flow over a permeable stretching sheet in the presence of a magnetic field. The findings highlighted that both suction and injection significantly affect the velocity and temperature profiles of the fluid, with potential applications in controlling the cooling rates in polymer processing and other industrial manufacturing processes. This study provided insights into how manipulating the boundary conditions can optimize heat and mass transfer in stretching sheet applications.

Kinyanjui et al. (2012) focused on the effects of radiation and heat generation on MHD free convection flow past an inclined stretching sheet. The results demonstrated that radiation and internal heat generation considerably influence the thermal boundary layer thickness and the surface heat transfer rate. The study concluded that these factors must be accounted for in the design of thermal systems involving stretching surfaces, such as those used in aerospace and electronic cooling applications.

The study of fluid flow through porous media in a rotating system has also garnered significant interest due to its applications in fields such as petroleum engineering, geothermal energy systems, and hydrology. Understanding the behavior of these flows can help optimize processes like oil and gas recovery and the spread of pollutants in groundwater. Recent studies have delved deeper into the complexities of hydromagnetic turbulent flow in such systems.

Chamkha et al. (2019) explored magneto-hydrodynamic flow and heat transfer of a hybrid nanofluid in a rotating system between two surfaces, revealing that the Nusselt and Reynolds numbers are directly related for injection flow cases, while higher values of the suction parameter result in an inverse relationship. Krishna et al. (2021) investigated unsteady MHD convective rotating flow past an infinite vertical moving porous surface, noting that the Hartmann number and the resultant velocity are inversely related.

Sharma et al.(2021) studied hydromagnetic boundary layer flow with heat transfer past a rotating disc embedded in a porous medium, finding that the Coriolis force significantly impacts axial flow, with an increase in the Prandtl number enhancing heat transfer. Negi et al. (2023) further conducted a numerical analysis of fluid flow and heat transfer between two rotating disks with an induced porous medium, observing that the tangential velocity profile increases uniformly with higher stretching parameter values.

The study of hydromagnetic turbulent flow in porous media over a stretching surface within a rotating system, combined with heat transfer, is crucial for advancing both theoretical knowledge and practical applications in various fields. Turbulent flows are not only common in natural processes like atmospheric and oceanic circulation but are also integral to industrial activities such as mixing in chemical reactors and pipeline flow. The examination of fluid movement through porous materials has significant implications for engineering and environmental applications, including groundwater flow, oil recovery, and filtration systems.

Understanding how rotation affects flow patterns and heat transfer is vital for improving the design and efficiency of engineering systems, from rotating machinery to atmospheric circulations. Additionally, heat transfer dynamics, when studied alongside fluid flow in porous media, provide valuable insights into the thermal behavior of systems like geothermal reservoirs and electronic cooling setups. The integration of magnetic fields into this analysis further enhances the study's relevance, particularly in areas such as magnetohydrodynamics (MHD). This research is poised to influence the development of more efficient and environmentally friendly engineering systems that involve fluid flow, porous materials, rotation, heat transfer, and magnetic fields across a wide range of industrial and environmental applications.

Despite various investigations on fluid flow there is a distinct lack of research on hydromagnetic turbulent flow in porous media over a stretching surface within a rotating system with heat transfer which forms the basis for this study.

Mathematical Analysis.

The orientation as shown in Figure **1** is established with the z-axis along the plate, y-axis perpendicular to the plate, and x-axis perpendicular to the y-z plane. The plate is infinite along the x and z axes, with a uniform transverse magnetic field applied parallel to the y-axis.

Figure 1: Flow Configuration

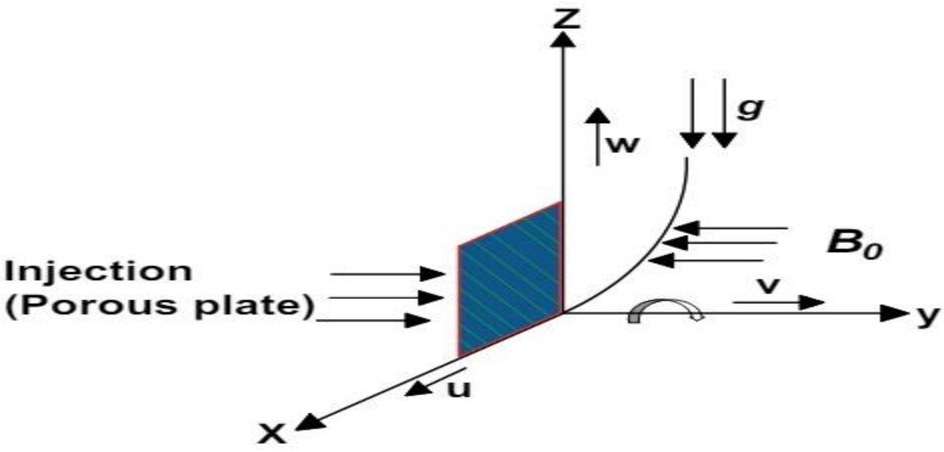

Building on this setup, this chapter presents the equations governing hydromagnetic turbulent flow in porous media over a stretching surface within a rotating system with heat transfer. These equations take into account key assumptions: the fluid flow is restricted to the turbulent domain, properties such as electrical conductivity, thermal conductivity, and viscosity are constant, and the influence of the electric field is negligible compared to the Lorentz force. The porous medium and fluid are assumed to be in local thermal equilibrium, with the no-slip condition applying at the boundary. Based on these considerations, the momentum and energy equations are formulated and expressed using non-dimensional parameters to emphasize the significance of each factor in the flow dynamics.

Equation of motion

The general equation of motion in tensor form is written as;

$$\rho\left(\frac{\partial u_i}{\partial t}+u_j\frac{\partial u_i}{\partial x_j}\right)+2\Omega u_i=-\frac{\partial p}{\partial x_i}+\mu\,\nabla^2 u_i+F_i \qquad \textbf{(1)}$$

where $i, j = 1, 2, 3$ are the summation variables along x, y, and z directions respectively.

The left-hand side of the equation **(1)** includes three terms: local (temporal) acceleration, convective acceleration (change in velocity with respect to distance), and Coriolis acceleration. On the right-hand side, the terms represent the pressure gradient, viscous force, and body force, respectively. This equation illustrates how body forces and surface forces are balanced by the rate of change of momentum.

When viewed from a rotating frame of reference, moving objects appear to deviate from a straight path due to the Coriolis force. For a system rotating at a constant angular velocity about the y-direction, the magnitude and direction of the Coriolis acceleration is given by;

$$2\boldsymbol{\Omega}\times\boldsymbol{q}=\begin{vmatrix}\boldsymbol{i} & \boldsymbol{j} & \boldsymbol{k}\\ 0 & 2\boldsymbol{\Omega} & 0\\ u & v & w\end{vmatrix}=$$

$$2\boldsymbol{\Omega}w\boldsymbol{i}-2\boldsymbol{\Omega}u\boldsymbol{k} \qquad \textbf{(2)}$$

Where $q(u, v, w)$ is the velocity vector while $\boldsymbol{\Omega}$ is the angular velocity

Additionally, Lorentz force component is given by:

$$(J\times B)_x=\frac{\sigma B_0^2(mu+w)}{1+m^2} \qquad \textbf{(3)}$$

$$(J\times B)_z=\frac{\sigma B_0^2(mw-u)}{1+m^2} \qquad \textbf{(4)}$$

Momentum Equation in the z-Direction & x-direction

The general equation of motion along the z-direction takes the form

$$\frac{\partial w}{\partial t}+v_0\frac{\partial w}{\partial y}+w\frac{\partial w}{\partial z}-2\mathbf{\Omega}u = v\nabla^2 w+\beta g(T-T_\infty)-\frac{\sigma \boldsymbol{B}_{\mathbf{0}}^{\mathbf{2}}(mw-u)}{\rho(1+m^2)}-\frac{\mu}{\gamma}w \quad \textbf{(5)}$$

Equation **(5)** describes the momentum balance in the z-direction, accounting for temporal and convective accelerations, Coriolis effects, pressure gradients, viscous forces, and the Lorentz force components.

Additionally, the equation of motion along the x-axis takes the form:

$$\frac{\partial u}{\partial t}+v_0\frac{\partial u}{\partial y}+w\frac{\partial u}{\partial z}+2\Omega w=v\nabla^2 u-\frac{\sigma B_0^2(mu+w)}{\rho(1+m^2)}-\frac{\mu}{\gamma}u \quad \textbf{(6)}$$

This equation **(6)** describes the momentum balance in the x-direction, also accounting for similar factors including temporal and convective accelerations, Coriolis effects, pressure gradients, viscous forces, and Lorentz force components.

Energy Equation

This equation is derived from the first law of thermodynamics which states that energy is conserved in process involving a thermodynamic system and its surrounding. Mathematically, this law is defined as

$$C_p\left(\frac{D\rho}{Dt}+\rho\nabla T\right)=k\nabla^2 T+\mu\phi+\frac{J^2}{\sigma}+\nabla.\boldsymbol{Q}r \quad \textbf{(7)}$$

where $\frac{J^2}{\sigma}$ represents joule heating, and $\nabla.\boldsymbol{Q}r$ denotes the radiating heat flux. C_p is the specific heat capacity at a constant pressure, $k\nabla^2 T$ is the heat conduction and $\frac{D}{Dt}$ is the material derivative and is expressed as:

$$\frac{D}{Dt}=\frac{\partial}{\partial t}+u\frac{\partial}{\partial x}+v\frac{\partial}{\partial y}+w\frac{\partial}{\partial z} \quad \textbf{(8)}$$

And the energy equation takes the form;

$$\rho C_\rho\left(\frac{\partial T}{\partial t}+v_0\frac{\partial T}{\partial y}+w\frac{\partial T}{\partial z}\right)=k\nabla^2 T+\mu\left(\left(\frac{\partial u}{\partial y}\right)^2+\left(\frac{\partial w}{\partial y}\right)^2\right) +\sigma B_0^2\left[\frac{(mu+w)^2+(mw-u)^2}{(1+m^2)^2}\right] \quad \textbf{(9)}$$

Time Averaged Momentum Equation

Our z-direction momentum equation is

$$\frac{\partial w}{\partial t}+v_0\frac{\partial w}{\partial y}+w\frac{\partial w}{\partial z}-2\Omega u = v\nabla^2 w+\beta g(T-T_\infty)-\frac{\sigma B_0^2(mw-u)}{\rho(1+m^2)}-\frac{\mu}{\gamma}\,w \tag{10}$$

In terms of time average quantities, equation **(10)** yields:

$$v\nabla^2\bar{w}+v\nabla^2 w'+\beta g(\bar{T}+T'-T_\infty) -\frac{\sigma B_0^2\big(m(\bar{w}+w')-(\bar{u}+u')\big)}{\rho(1+m^2)}-\frac{\mu(\bar{w})}{\gamma}-\frac{\mu(w')}{\gamma} \tag{11}$$

Similarly, the momentum equation along the x-direction is:

$$\frac{\partial\bar{u}}{\partial\bar{t}}+v_0\frac{\partial\bar{u}}{\partial\bar{y}}+\bar{w}\frac{\partial\bar{u}}{\partial\bar{z}}+2\Omega\bar{w} = v\nabla^2\bar{u}-\frac{\sigma B_0^2(m\bar{u}+\bar{w})}{\rho(1+m^2)}-\frac{\mu}{\gamma}\bar{u}-\frac{\overline{\partial u'v'}}{\partial y} \tag{12}$$

Time Average Energy Equation

$$\rho C_p\left(\frac{\partial T}{\partial t}+v_0\frac{\partial T}{\partial y}+w\frac{\partial T}{\partial z}\right)=k\,\nabla^2 T+\mu\left(\left(\frac{\partial u}{\partial y}\right)^2+\left(\frac{\partial w}{\partial y}\right)^2\right) +\sigma B_0^2\left[\frac{(mu+w)^2+(mw-u)^2}{(1+m^2)^2}\right] \tag{13}$$

Using the normal time averaging and RANS equation the above equation reduces to:

$$\rho C_p\left(\frac{\partial\bar{T}}{\partial\bar{t}}+v_0\frac{\partial\bar{T}}{\partial\bar{y}}+\bar{w}\frac{\partial\bar{T}}{\partial\bar{z}}\right)=k\nabla^2\bar{T}+\mu\left(\left(\frac{\partial\bar{u}}{\partial\bar{y}}\right)^2+\left(\frac{\partial\bar{w}}{\partial\bar{y}}\right)^2\right) +\sigma B_0^2\left[\frac{(m\bar{u}+\bar{w})^2+(m\bar{w}-\bar{u})^2}{(1+m^2)^2}\right] \tag{14}$$

Boussinesq Approximation

From Boussinesq approximation:

$$\tau_t=-\rho u'w'=\rho\varepsilon_m\left(\frac{\partial\bar{w}}{\partial z}\right) \tag{15}$$

Empirical methods are employed to address the Reynolds shear stress terms in Equation **(15),** which leads to the adoption of the Prandtl mixing length hypothesis. Prandtl made the assumption that the momentum is transported by eddies that moved in the z-direction over the distance l without interaction and then mixed with the existing fluid at the new locations. Thus, from experiments Prandtl deduced that:

$$\rho u'w' = -\rho l^2 \left(\frac{\partial \overline{w}}{\partial x}\right)^2 \tag{16}$$

Non-dimensional Analysis

Involves the process of identifying the fundamental units from the equation and constructing non-dimensional groups using these units, then writing these equations in terms of dimensionless elements. This process is important in fluid mechanics as it helps in identifying parameters that affect flow. Secondly, by using non-dimensional numbers, engineers can perform calculations on a small scale and then extrapolate the results to actual scenario. In this study, non-dimensionalisation is based on the following quantities:

$$t = \frac{\bar{t}W^2}{v}, x = \frac{\bar{x}W}{v}, y = \frac{\bar{y}W}{v}, z = \frac{\bar{z}W}{v}, v = \frac{\bar{v}}{W}, w = \frac{\overline{w}}{W}, u = \frac{\bar{u}}{W}, v_0 = \frac{\overline{v_0}}{W}, \theta = \frac{\overline{T} - T_\infty}{T_w - T_\infty}, H = \frac{\overline{H}}{H_0}$$

Equation of conservation of momentum

The equation of conservation of momentum in this type of flow along the z-axis and the x-axis respectively after adopting Boussinesq approximation is given by:

$$\begin{aligned}\frac{\partial \overline{w}}{\partial \bar{t}} + v_0 \frac{\partial \overline{w}}{\partial \bar{y}} + \overline{w}\frac{\partial \overline{w}}{\partial \bar{z}} - 2\Omega \bar{u} + v\left(\frac{\partial^2 \overline{w}}{\partial \bar{y}^2} + \frac{\partial^2 \overline{w}}{\partial \bar{z}^2}\right) + \beta g(\overline{T} - T_\infty) \\ - \frac{\sigma B_0^2 (m\overline{w} - \bar{u})}{\rho(1+m^2)} - \frac{\mu(\overline{w})}{\gamma} + 2\lambda^2 y \left(\frac{\partial w}{\partial y}\right)^2 \\ + \lambda^2 y^2 \left(\frac{\partial^2 w}{\partial y^2}\right)\left(\frac{\partial w}{\partial y}\right)\end{aligned} \tag{17}$$

$$\begin{aligned}\frac{\partial \bar{u}}{\partial \bar{t}} + v_0 \frac{\partial \bar{u}}{\partial \bar{y}} + \overline{w}\frac{\partial \bar{u}}{\partial \bar{z}} + 2\Omega \overline{w} \\ = v\left(\frac{\partial^2 \bar{u}}{\partial \bar{y}^2} + \frac{\partial^2 \bar{u}}{\partial \bar{z}^2}\right) - \frac{\sigma B_0^2 (m\overline{w} - \bar{u})}{\rho(1+m^2)} - \frac{\mu}{\gamma}\bar{u} \\ + 2\lambda^2 y \left(\frac{\partial u}{\partial y}\right)^2 + \lambda^2 y^2 \left(\frac{\partial^2 u}{\partial y^2}\right)\left(\frac{\partial u}{\partial y}\right)\end{aligned} \tag{18}$$

Non-dimensionalising the momentum equation along the z-axis, we get;

$$\frac{\partial \bar{w}}{\partial t}+v_0\frac{\partial w}{\partial y}+w\frac{\partial w}{\partial z}-2Ru$$
$$=\left(\frac{\partial^2 w}{\partial y^2}+\frac{\partial^2 w}{\partial z^2}\right)+Gr\theta-M\frac{(mw-u)}{(1+m^2)}-X_i w \qquad \textbf{(19)}$$
$$+\frac{v}{W^3}[2\lambda^2 y\left(\frac{\partial w}{\partial y}\right)^2+\lambda^2 y^2\left(\frac{\partial^2 w}{\partial y^2}\right)\left(\frac{\partial w}{\partial y}\right)$$

where $R=\frac{\Omega_v}{W^2}$ is the Rotation parameter, $Gr=\frac{g\beta(T_w-T_\infty)v}{W^3}$ is the Grashof number, $M=\frac{v\sigma B_0^2}{\rho W^2}$ is the Magnetic field parameter and $X_i=\frac{v^2}{\gamma W^2}$ is the permeability parameter.

Now, non-dimensionalising the momentum equation along the x-axis, we have:

$$\frac{\partial u}{\partial t}+v_0\frac{\partial u}{\partial y}+w\frac{\partial u}{\partial z}+2Rw$$
$$=\left(\frac{\partial^2 \bar{u}}{\partial \bar{y}^2}+\frac{\partial^2 \bar{u}}{\partial \bar{z}^2}\right)-M\frac{(mu+w)}{(1+m^2)}-X_i u \qquad \textbf{(20)}$$
$$+\frac{v}{W^3}\left[2\lambda^2 y\left(\frac{\partial u}{\partial y}\right)^2+\lambda^2 y^2\left(\frac{\partial^2 u}{\partial^2}\right)\left(\frac{\partial u}{\partial y}\right)\right]$$

Where $R=\frac{\Omega v}{W^2}$ is the Rotation parameter, $M=\frac{v\sigma B_0^2}{\rho W^2}$ is the Magnetic field parameter and

$X_i=\frac{v^2}{\gamma W^2}$ is the permeability parameter.

Energy Equation

Non-dimensionalising the energy equation **(14), we obtain,**

$$\frac{\partial \theta}{\partial t}+v_0\frac{\partial \theta}{\partial y}+w\frac{\partial \theta}{\partial z}$$
$$=\frac{1}{Pr}\left(\frac{\partial^2 \theta}{\partial y^2}+\frac{\partial^2 \theta}{\partial z^2}\right)+Ec\left[\left(\frac{\partial u}{\partial y}\right)^2+\left(\frac{\partial w}{\partial y}\right)^2\right] \qquad \textbf{(21)}$$
$$+J_0\left[\frac{(mu+w)^2+(mw-u)^2}{(1+m^2)^2}\right]$$

where $Pr=\frac{\mu C_p}{k}$ is the Prandtl Number, $Ec=\frac{W^2}{C_p(T_w-T_\infty)}$ is the Eckert number,

$J_0=\frac{\sigma B_0^2\mu}{\boldsymbol{\rho^2 C_p(T_w-T_\infty})}$ is the joule heating parameter.

The non-dimensional form for the initial and boundary conditions for this study are:

$t \leq 0 \quad w(y,t) = 0 \quad u(y,t) = 0 \quad \theta(y,t) = 0$

$t \geq 0 \quad w(y,t) = 1 \quad u(0,t) = 0 \quad \theta(0,t) = 1$

$w(\infty,t) = 0 \quad u(\infty,t) = 0 \quad \theta(\infty,t) = 0$

Method of solution

We obtained our results by applying three finite difference equations: the momentum equation in the z-axis (Equation 22), the momentum equation in the x-axis (Equation 23), and the energy equation (Equation 24).

Equation of momentum in z-axis

$$\begin{aligned} w_{i,j+1} = w_{i,j} - v_0 k \frac{w_{i+1,j} - w_{i,j}}{h} + 2kRu_{i,j} \\ + \frac{k}{h^2}\left[w_{i+1,j} - 2w_{i,j} + w_{i-1,j}\right] w\_(i + 1 + Gr\theta_{i,j}k \\ - \frac{Mk}{(1+m^2)}\left(mw_{i,j} - u_{i,j}\right) - X_i w_{i,j} k \\ - \frac{vk}{W^3}\left[2\lambda^2 y \left(\frac{w_{i+1,j} - w_{i,j}}{h}\right)^2 \right. \\ \left. + \lambda^2 y^2 \left(\frac{w_{i+1,j} - 2w_{i,j} + w_{i-1,j}}{h^2}\right)\left(\frac{w_{i+1,j} - w_{i,j}}{h}\right)\right] \end{aligned} \quad \textbf{(22)}$$

The momentum equation in the x-axis

$$\begin{aligned} u_{i,j+1} = u_{i,j} - v_0 k \frac{u_{9i} + 1, j) - u_{i,j}}{h} - 2kRw_{i,j} \\ + \frac{k}{h^2}\left(u_{i+1,j} - 2u_{i,j} + u_{i-1,j}\right) \\ - \frac{Mk}{(1+m^2)}\left(mu_{i,j} + w_{i,j}\right) - X_i u_{i,j} k \\ + \frac{vk}{W^3}\left[2\lambda^2 y \left(\frac{u_{i,j+1} - u_{i,j}}{k}\right)^2 \right. \\ \left. + \lambda^2 y^2 \left(\frac{u_{i+1,j} - 2u_{i,j} + u_{i-1,j}}{h^2}\right)\left(\frac{u_{i,j+1} - u_{i,j}}{k}\right)\right] \end{aligned} \quad \textbf{(23)}$$

The energy equation

$$\begin{aligned} \theta_{i,j+1} = \theta_{i,j} - v_0 k \frac{\theta_{i+1,j} - \theta_{i,j}}{h} + \frac{k}{Pr}\left(\frac{\theta_{i+1,j} - 2\theta_{i,j} + \theta_{i-1,j}}{h^2}\right) \\ + Ec\left[\left(\frac{u_{i+1,j} - u_{i,j}}{h}\right)^2 + \left(\frac{w_{i+1,j} - w_{i,j}}{h}\right)^2\right] k \\ + \frac{J_0 k}{(1+m^2)^2}\left[\left(mu_{i,j} + w_{i,j}\right)^2 + \left(mw_{i,j} - u_{i,j}\right)^2\right] \end{aligned} \quad \textbf{(24)}$$

Where;

i and j correspond to the variables y and t respectively, During computaion, Δy is taken as 0.1 and Δt is taken as 0.02 . The initial conditions in the above equations take the form:

$w(i,1) = 1, u(i,1) = 0$ and $\theta(i,1) = 0$

The boundary conditions for $y = 0$ in the above equation **(22), (23)** and **(24)** are:

$w(1,j) = 1, u(1,j) = 0$ and $\theta(1,j) = 1$

Results

In this chapter, the results of the simulation are presented, followed by discussions to provide a deeper understanding of the effects of varying dimensionless parameters on the velocity and temperature fields. The primary focus is on how these parameters influence the fluid dynamics and thermal characteristics of the flow. Specifically, the analysis considers the effects of the Grashof number (Gr = 0.5, 1.0, 1.5), Joule heating parameter ($J_o = 0.1, 0.2, 0.3$), Rotational parameter ($R = 0.5, 0.6, 0.7$), Permeability parameter ($X_i = 1, 1.5, 2.0$), Eckert number ($E_c = 0.01, 0.02, 0.05$), and Magnetic field parameter ($M = 0.1, 0.25, 0.5$). The analysis distinguishes between primary and secondary velocities, corresponding to the z-axis and x-axis directions, respectively. Through numerical computations, the chapter reveals how changes in these dimensionless parameters affect the flow characteristics. The unsteady flow results, presented in the form of graphs, highlight these dependencies and illustrate the complex interactions within the system.

Effect of varying Grashof number, Gr, on velocity and temperature profile

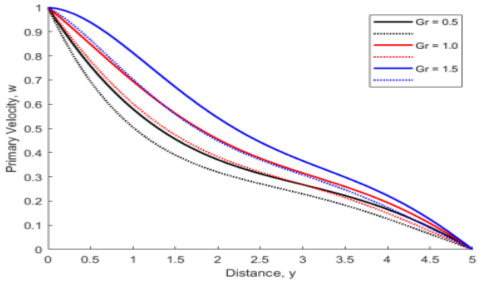

Figure 2: Primary velocity profiles of varying Gr, Gr=0.5, 1.0, and 1.5

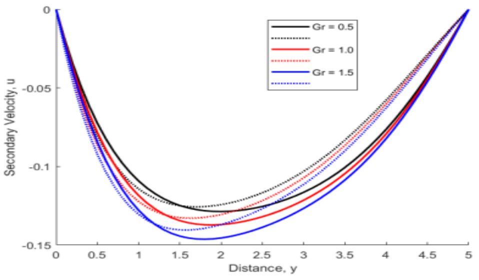

Figure 3: Temperature profiles of varying Gr, Gr = 0.5, 1.0, and 1.5

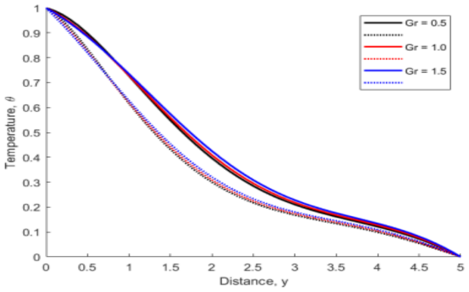

Figure 4: Secondary velocity profiles

for different Values of Gr=0.5, 1.0, and 1.5

As shown in Figure 2, increasing the Grashof number boosts primary velocity, highlighting stronger buoyancy forces that assist fluid flow. Figure 3 indicates a decrease in secondary velocity near the plate, but it rises further away due to a thinning momentum boundary layer.

Figure 4 shows that while temperature initially decreases near the plate with a higher Grashof number, it starts increasing beyond a distance of 1.0, reflecting enhanced heat transfer. Overall, a higher Grashof number increases primary velocity and temperature while causing complex changes in secondary velocity.

Effect of varying Joule heating parameter, Jo, on velocity and temperature profiles

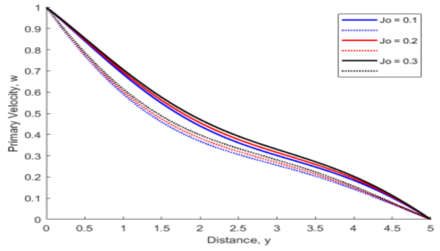

Figure 5: Primary velocity profiles of varying Jo, Jo = 0.1, 0.2, and 0.3

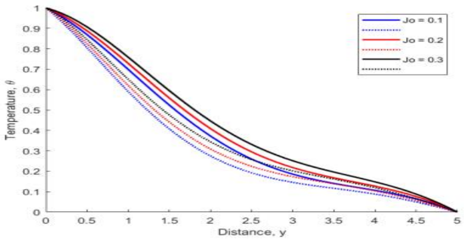

Figure 7: Temperature profiles of varying Jo, Jo=0.1, 0.2, and 0.3

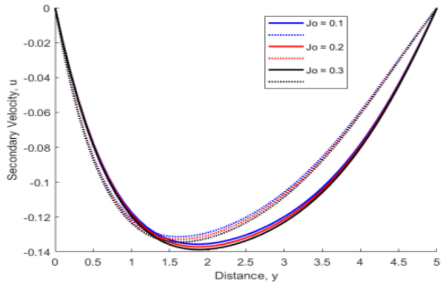

Figure 6: Secondary velocity profiles for different values of Jo, Jo =0.1, 0.2, and 0.3

Figure 5 shows that increasing the Joule heating parameter leads to a rise in primary velocity, as the heat generated reduces the fluid's viscosity or increases its buoyancy, enhancing the main flow. Figure 6 illustrates that the secondary velocity decreases with higher Joule heating but begins to increase beyond a distance of 2.0 from the plate, where the momentum boundary layer thins and viscosity effects lessen. Figure 7 indicates that increased Joule heating raises the temperature profile, as the added thermal energy elevates the overall fluid temperature

Effect of varying Rotational parameter, R, on velocity and temperature profiles

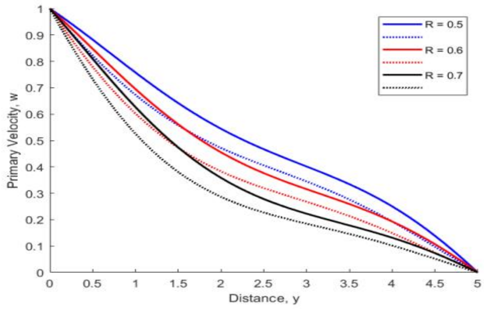

Figure 8: Primary velocity profiles of varying R, R=0.5, 0.6, and 0.7

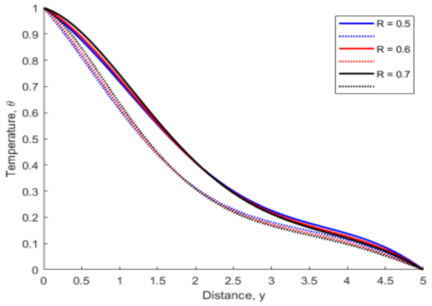

Figure 10: Temperature profiles of varying R, R=0.5, 0.6, and 0.7

Figures 8 and 9 demonstrate that increasing the rotational parameter R leads to a decrease in both primary and secondary velocities. A higher rotational parameter indicates that the Coriolis force, acting perpendicular to the fluid motion, becomes stronger than the inertial force, adding resistance to the flow. This results in increased effective viscosity, which slows down the fluid, reducing both primary and secondary velocities. Figure 10 shows that as the rotational parameter increases, the temperature profile rises near the plate but begins to decrease beyond a distance of 2.0. The oscillation frequency increases the temperature near the plate, where the thermal boundary layer is thicker, but as the fluid moves away from the heated plate, the boundary layer thins, leading to a drop in temperature.

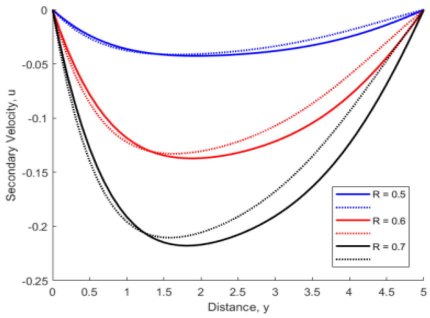

Figure 9: Secondary velocity profiles for different values of R, R=0.5, 0.6, and 0.7

Effect of varying Eckert number, Ec, on velocity and temperature profiles

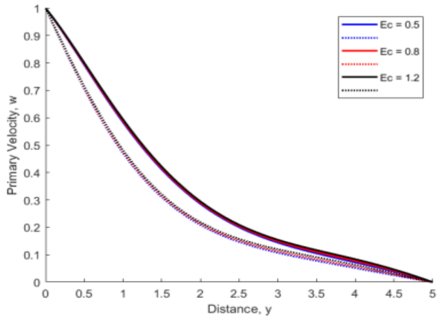

Figure 11: Primary velocity profiles of varying Ec, Ec=0.5, 0.8, and 1.2

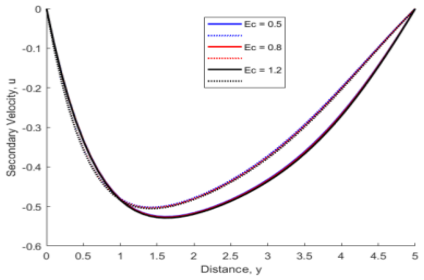

Figure 12: Secondary velocity profiles for different values of Ec, Ec=0.5, 0.8, and 1.2

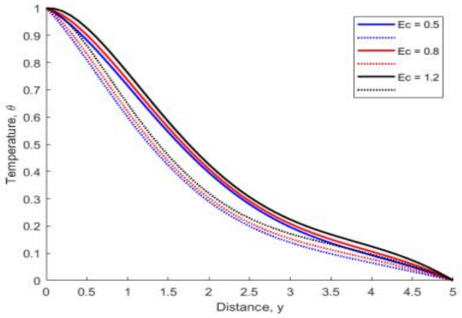

Figure 13: Temperature profiles of varying Ec, Ec=0.5, 0.8, and 1.2

An increase in the Eckert number, as shown in Figure 11, raises the fluid's kinetic energy, resulting in higher primary velocity. As Figure 12 illustrates, the secondary velocity decreases near the plate due to a thicker momentum boundary layer but increases further away. Figure 13 confirms that this increase in heat absorption elevates the temperature profiles, indicating a cooling effect on the porous plate.

Effect of varying Permeability parameter, Xi, on velocity and temperature profiles

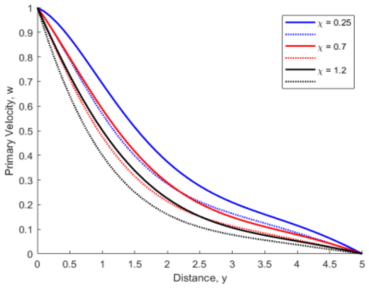

Figure 14: Primary velocity of varying Xi, Xi=0.25, 0.7, and 1.2

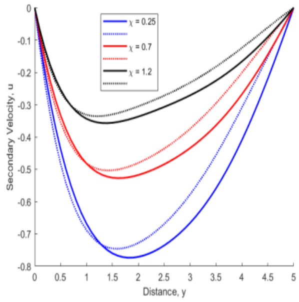

Figure 15: Secondary velocity profiles for different values of Xi, Xi=0.25, 0.7, and 1.2

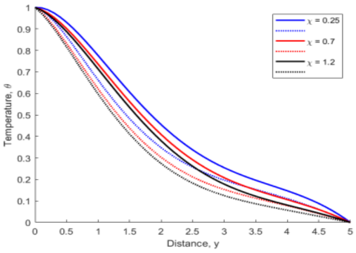

Figure 16: Temperature profiles of varying Xi, Xi=0.5, 0.8 and 1.2

Figures 14 through 16 illustrate the effects of increasing the Permeability parameter X_i, which inversely relates to the actual permeability k of the porous medium. As X_i increases, the plate's porosity enhances, leading to higher fluid viscosity near the plate. This results in reduced flow acceleration, causing a decrease in primary velocity (Figure 14). The secondary velocity initially rises near the plate and experiences a sharper increase further away (Figure 15). However, the overall pressure drop weakens, reducing the secondary velocity. This reduced acceleration decreases heat transfer, leading to a lower temperature profile (Figure 16).

Effect of varying Magnetic field parameter, M, on velocity and temperature profiles

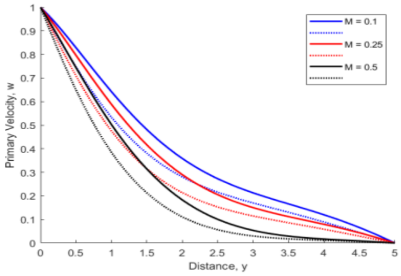

Figure 17: Primary velocity profiles of varying M, M=0.1, 0.25, and 0.5

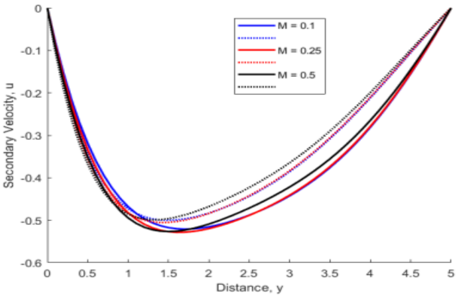

Figure 18: Secondary velocity profiles for different values of M=0.1, 0.25, and 0.5

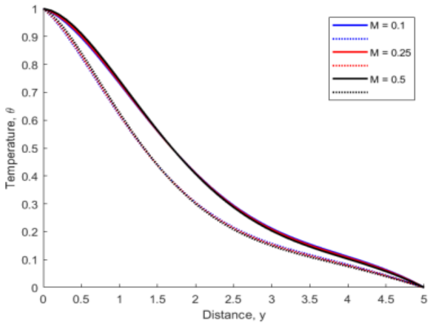

Figure 19: Temperature profiles of varying M, M=0.1, 0.25, and 0.5

Figures 17 and 18 illustrate that as the Magnetic field parameter (M) increases, the primary velocity decreases, while the secondary velocity decreases near the plate but increases away from it, particularly at the crossover point around 1.2. Figure 19 shows that with increasing M, the temperature profile rises near the plate but begins to decrease beyond the crossover at 1.5. This behavior is explained by the introduction of a strong magnetic field perpendicular to the flow of an electrically conducting fluid, generating an induced electric current. The interaction between the current and magnetic field creates a Lorentz force, which resists fluid motion, reducing primary velocity. The secondary velocity increases away from the plate due to the thinning momentum layer. Additionally, the stronger Lorentz force leads to significant Joule heating, increasing the temperature near the plate until it decreases after the crossover point

Discussion

The results presented highlight the intricate interactions between various dimensionless parameters and their impact on velocity and temperature profiles in hydromagnetic turbulent flow within porous media. The increase in primary velocity with higher Grashof numbers, as shown in Figure 2, underscores the significant role of buoyancy forces in enhancing fluid flow. This finding is consistent with theoretical expectations that buoyancy-driven flows can accelerate fluid movement.

Similarly, the observed decrease in secondary velocity near the plate (Figure 3) followed by an increase further away is attributed to the thinning of the momentum boundary layer. This behavior is crucial for optimizing cooling processes in industrial applications, where control over boundary layer dynamics can improve heat transfer efficiency.

The effect of Joule heating, which leads to higher primary velocity and temperature (Figures 5 - 7), highlights the role of thermal energy in altering fluid viscosity and buoyancy. This finding is particularly relevant for applications involving electrical heating in fluids, such as in metal cooling processes.

Rotation, represented by the rotational parameter (Figures 8 -10), introduces additional resistance to the flow due to the stronger Coriolis force. This effect must be carefully managed in systems where rotational forces play a significant role, such as in rotating machinery and atmospheric studies.

Finally, the impact of the magnetic field parameter on velocity and temperature profiles (Figures 17-19) demonstrates how magnetic forces can influence fluid behavior, offering insights into applications involving magnetohydrodynamics, such as in nuclear reactors and space propulsion systems.

Conclusion and Recommendation

The study provides valuable insights into how various dimensionless parameters affect hydromagnetic turbulent flow and heat transfer. Future research should focus on a detailed exploration of these effects, particularly in relation to the specific objectives of optimizing flow and heat transfer in industrial applications. Further investigation into the combined effects of these parameters will enhance our understanding and lead to more effective and efficient design strategies in relevant engineering fields.

Disclaimer (Artificial intelligence)

Option 1:

Author(s) hereby declare that NO generative AI technologies such as Large Language Models (ChatGPT, COPILOT, etc) and text-to-image generators have been used during writing or editing of manuscripts.

Option 2:

Author(s) hereby declare that generative AI technologies such as Large Language Models, etc have been used during writing or editing of manuscripts. This explanation will include the name, version, model, and source of the generative AI technology and as well as all input prompts provided to the generative AI technology

Details of the AI usage are given below:

1.

2.

3.

References

al., S. e. (2021). Hydromagnetic boundary layer flow with heat transfer past a rotating disc embedded in a porous medium. Heat Transfer, 50(5), 4342-4353.

Chamkha et al. (2019). Magneto-hydrodynamic flowand heat transfer of a hybrid nanofluid in a rotating system among two surfaces in the presence of thermal radiation and Joule heating. AIP Advances, 9(2).

Giterere, K. E. (2013). Magnetohydrodynamic flow in porous media over a stretching surface in a rotating system with heat and mass transfer. *Doctoral Dissertation*.

Kinyanjui et al. (2012). Hydromagnetic turbulent flow of a rotating system past a semi-infinite vertical plate with Hall current. *International Journal of Heat and Mass Transfer*, 97-119.

Krishna et al. (2021). Numerical investigation on unsteady MHD convective rotating flow past an infinite vertical moving porous surface. *Ain Shams Engineering Journal, 12(2), 2099-2109.*

Kumari & Gorla. (2015). Heat and Mass Transfer in a Nanofluid Film on an Unsteady Stretching Surface. *Journal of Nanofluids*, 560-567.

Mahapatra & Gupta . (2004). Stagnation-point flow of a viscoelastic fluid towards a stretching surface. *International Journal of Non-Linear Mechanics*, 811-820.

Negi et al. (2023). A numerical analysis of fluid flow and heat transfer between two rotating disks with induced porous medium. Numerical Heat Transfer, Part B: Fundamentals. 1-16.

Ngari, D. N. (2017). urbulent Hydromagnetic Flow with Radiative Heat over Moving Vertical Porous Plate in a Rotating System. *Doctoral dissertation*.

Sharma et al. (2021). Hydromagnetic boundary layer flow with heat transfer past a rotating disc embedded in a porous medium. Heat Transfer, 50(5), 4342-4353.

Singh & Jha. (2013). A Periodic Solution of Oscillatory Couette MHD Flow Through Porous Medium in Rotating System. 01-09.

Srihari, K. (2021). Heat Transfer Flow Over a Heated Stretching Sheet in the Presence of a Magnetic Field.